2021-04-29

Probing the application of kinetic theory to Mg-phyllosilicate growth with Si isotope doping

Che, Zhengqiang

UNIVERSITY OF CALGARY

Probing the application of kinetic theory to Mg-phyllosilicate growth with Si isotope doping

by

Zhengqiang Che

A THESIS

SUBMITTED TO THE FACULTY OF GRADUATE STUDIES

IN PARTIAL FULFILMENT OF THE REQUIREMENTS FOR THE

DEGREE OF MASTER OF SCIENCE

GRADUATE PROGRAM IN GEOSCIENCE

CALGARY, ALBERTA

APRIL, 2021

Abstract

The Principle of Detailed Balance (PDB) played a defining role in the derivation of the widely-used Transition State Theory rate law equation and serves as an important link between geochemical kinetics and thermodynamics. Although significant improvements have been made in applying the PDB to comparatively simple systems (e.g., SiO_2-water), experimental verification of the PDB is lacking for more complex minerals such as the phyllosilicates. Among them, Mg-phyllosilicates are particularly important and have profound implications for the construction of facies models, element cycling in the lacustrine/marine realm, and interpretation of paleo-biogeochemistry. Here, we use ^{29}Si isotopic doping techniques to quantify the rates of reaction between Mg-phyllosilicate substrates (amorphous Mg-silicate (a talc-like phase) and crystalline talc) and supersaturated solutions. The results show that the ratio of the forward and backward rates of amorphous Mg-silicate-water reaction approaches unity as the saturation state of the solution approaches the apparent solubility of amorphous Mg-silicate. The precipitation rates coupled with equivalent dissolution rates (in experiments with amorphous Mg-silicate substrates) appear to obey the same rate function as the precipitation rates coupled with negligible dissolution rates (in experiments with crystalline Mg-silicate substrates) over the degrees of supersaturation we explore, suggesting that the elementary step limiting the rate of precipitation remains the same. Accordingly, our results demonstrate that the PDB is applicable to amorphous Mg-phyllosilicate-water reactions, thereby reinforcing the use of TST rate equations to describe Mg-phyllosilicates growth. The experimental data can also be taken as evidence that the apparent solubility of amorphous Mg-silicate, a concept previously explained using the kinetic theory of nucleation and growth, also has a thermodynamic meaning, in that it represents a metastable equilibrium with the poorly crystalline phase. The measured, non-negligible forward and backward rates suggest that, even in this metastable state where little if any net reaction is occurring, isotopic signatures can be

reset. Moreover, the significant discrepancy between the heterogeneous net growth rates on the amorphous Mg-silicate substrate versus those measured on crystalline talc and sepiolite substrates indicates that mineral crystallinity likely plays a key role in mineral growth during diagenesis.

Acknowledgments

Throughout the journey as an international MSc student, I have received a great deal of support and assistance. First, I would like to thank my esteemed supervisor, Dr. Ben Tutolo, whose profound expertise was invaluable in conceiving this project, assisting the analyses, and improving the manuscript. His great passion and insightful views for science not only guided me during this wonderful scientific journey we have been together but also will encourage me in the future adventure that I am going to explore.

Particularly, I am extremely grateful to Mike Nightingale for his tremendous efforts throughout this project in developing and performing ICP-OES and ICP-MS analyses. I would also like to thank Jian Jun Li for the help with FTIR analyses, Robert Marr for the help with XRD analyses, and Dr. Yury Klyukin for the help with Raman analyses.

I acknowledge the support for this study and related research from the Natural Sciences and Engineering Research Council of Canada and Canada's Oil Sands Innovation Alliance under Collaborative Research and Development Grant number 532379-2018. The TQ-ICP-MS instrument was purchased with funds from the Canada First Research Excellence Fund.

A very large thank you goes to Dr. Bernhard Mayer and Dr. Mike Wieser for agreeing to be on my thesis examination committee. Their insightful feedback has pushed me to sharpen my thinking and bring my work to a higher level. I also thank Dr. Chen Zhu and five anonymous reviewers for reading the manuscript version and providing extensive and useful comments that helped to improve the content and clarity of the text.

Finally, I also appreciate all my friends, colleagues, and family members. Especially Qin Zhang, Yihua Liu, my previous and current housemates, etc. Without their tremendous support and encouragement throughout, it would be impossible for me to live abroad alone and complete this project.

Table of Contents

List of tables

List of figures

and the Q-ICP-MS measurement. The line shows a 1:1 relationship.

Fig S3 X-ray diffraction analysis of the crystalline talc used in the experiments.

Fig S4 Logarithm of precipitation rates as a function of the logarithm of ion activity product (Q) to sepiolite from Expt. IJ and Arizaleta et al. (2020).

1. Introduction

The Principle of Detailed Balance (PDB) is the foundation of Transition State Theory (TST) rate laws that have been applied to the calculation of water-rock reactions across the discipline of geology (Lasaga, 1981; Aagaard and Helgeson, 1982; Lasaga, 2014). It states, simply, that the forward and backward rates of a chemical reaction are equal at thermodynamic equilibrium (this is also referred to as microscopic reversibility). Based on this concept, the relationship between the equilibrium constant K_{eq} and the forward and backward rate constant (k^+ and k^-, respectively) for an elementary reaction can be described as $K_{eq} = k^+/k^-$. Assuming that this relationship is valid not only at equilibrium but also far from it, the widely adopted net dissolution and precipitation TST rate law $r = k \cdot f(\Omega)$ then can be derived mathematically (Lasaga, 1981; Aagaard and Helgeson, 1982; Lasaga, 2014), as discussed below.

1.1 Experimental validation of the Principle of Detailed Balance in geochemical rate theory

Despite more than one hundred years of PDB theory across the chemical sciences (Wegscheider, 1911), the range of its applicability to mineral-water interactions has not been directly tested experimentally until quite recently. Liu et al. (2016), by applying the isotope doping method, first simultaneously measured the forward and backward rates of quartz-water reactions at equilibrium at 50 °C with the pH around 5.5. These measurements proved unequivocally that the forward reaction constant k^+ of quartz dissolution at far-from-equilibrium conditions is virtually the same as it is at equilibrium. Moreover, the equilibrium constant calculated by $K_{eq} = k^+/k^-$ for quartz dissolution also matches the data determined by Rimstidt (1997). Nevertheless, because of the sheer abundance of multicomponent silicates in Earth's crust (~70% of the silicates in Earth's crust is comprised of multicomponent silicates(Deer, 1966; Earle, 2019)), and the comparatively simplistic composition and structure

of quartz in relation to these minerals, more detailed experimental investigations of PDB on other multicomponent phases are necessary to establish the limits of its applicability (Liu et al., 2016). Zhu et al. (2020) provided an important step towards testing the broader applicability of the PDB to multicomponent silicate dissolution by performing near-equilibrium albite and K-feldspar dissolution experiments at 50 °C using the isotope doping method. Their results suggest that microscopic reversibility is inapplicable to feldspar-water reactions at low temperature because of the absence of backward reaction products. Rather, the enrichment of Na, Al, and silicic acid led to the precipitation of a secondary Al, Si-bearing phase, which is in agreement with the concept of incongruent dissolution that states the mineral dissolves in the presence of a liquid and converts one solid phase into another. This, in turn, implies a lack of fundamental theoretical support for the applicability of the TST rate law to feldspar-water reactions at ambient temperature.

1.2 Mg-phyllosilicates as a model system for validating the applicability of the PDB

The abundance and reactivity of authigenic Mg-phyllosilicate minerals on Earth's surface (Pozo and Galán, 2015; Tosca, 2015) suggest that their behavior, and the applicability of the PDB to their behavior, may differ from that observed for the feldspars. Al-poor Mg phyllosilicates – including sepiolite ($Mg_4Si_6O_{15}(OH)_2(OH_2)_2*4H_2O$), stevensite ($M^+_{2y} \cdot nH_2O)(Mg_{3-y\square y}Si_4O_{10}(OH)_2$), where M indicates the exchangeable cation of the interlayers, □ dictates y vacancies, and n is variable, talc ($Mg_3Si_4O_{10}(OH)_2$), and kerolite ($Mg_3Si_4O_{10}(OH)_2*H_20$)– and their amorphous precursors (termed as amorphous Mg-silicate or Mg-silicate gel), are abundant not only in the geological record and modern natural environments (Pozo and Galán, 2015), but also in geothermal production operations (Gunnarsson et al., 2002; Spinthaki et al., 2018). In addition, the formation of Mg-silicate gelis relatively straightforward to examine experimentally (Brady, 1992; Tosca et al., 2011; Tosca and Masterson, 2014; Tosca, 2015; Tutolo et al., 2018; Tutolo and Tosca, 2018; Arizaleta et al.,

2020; Chase et al., 2021). For these reasons, Al-poor Mg-phyllosilicates serve as an opportune model system for exploring phyllosilicate-water interactions and the applicability of the PDB and TST rate laws to them.

Al-poor Mg-phyllosilicates are thought to initially precipitate as amorphous or gel-like phases before ultimately crystallizing with burial and heating (Tosca et al., 2011; Tosca and Masterson, 2014; Chase et al., 2021). Numerous experimental studies examining the dependence of nucleation and growth of amorphous Mg-phyllosilicates on various aspects of solution composition have been conducted over the past 50 or so years (Wollast et al., 1968; Kent and Kastner, 1985; Gunnarsson et al., 2005; Tosca et al., 2011; Tosca, 2015; Baldermann et al., 2018; Tutolo and Tosca, 2018; Arizaleta et al., 2020; Chase et al., 2021). These studies, combined with field measurements of fluid chemistry from Mg-silicate precipitating Lake Yoa (Darragi and Tardy, 1987) have permitted the delineation of a critical supersaturation for Mg-silicate nucleation from solution at Earth surface conditions, which, in effect, defines an effective solubility of amorphous Mg phyllosilicates (Tosca et al., 2011; Tosca, 2015; Tutolo and Tosca, 2018; Arizaleta et al., 2020; Chase et al., 2021). Below this threshold, Mg-phyllosilicate growth is still thermodynamically favorable, but direct, homogeneous nucleation is no longer favored.

To quantify the kinetics of heterogeneous Mg-phyllosilicate growth (i.e., growth at saturation states below the aforementioned critical supersaturation but still above equilibrium with respect to the crystalline phase), Arizaleta et al. (2020) performed a series of batch experiments using crystalline sepiolite as substrates to derive a heterogeneous growth rate law as a function of saturation state. This rate law was based on the general TST rate law, and its ability to describe the rate measurements thus provides indirect evidence of the applicability of the PDB to Mg-silicate growth. Importantly, however, this indirect evidence is not proof in and of itself of the applicability of the PDB, since the TST rate law can also be empirically

applied to mineral dissolution/growth (e.g., feldspar dissolution (Burch et al., 1993; Hellmann and Tisserand, 2006), with insignificant (i.e. immeasurable) microscopic reversibility near equilibrium at ambient conditions (Zhu et al., 2020)).

1.3 The application of PDB to Mg-silicate minerals and gels

To illustrate the application of the PDB to Mg-phyllosilicate-fluid reaction, we can take talc-water reactions as an example. Assuming that reactions are controlled by elementary chemical reactions, the forward and backward reaction can be written:

$$\mathrm{Mg_3Si_4O_{10}(OH)_2 + 6H^+ \Leftrightarrow 3Mg^{2+} + 4SiO_2(aq) + 4H_2O}\ . \quad (1)$$

Given that the dissolution of talc is a surface-controlled reaction (i.e., at far-from equilibrium conditions, the reaction is independent of solution saturation state (Saldi et al., 2007)) and that the precipitation rates of Mg-phyllosilicates are dependent on the ion activity product (Arizaleta et al., 2020), according to the PDB (Lasaga, 2014), the forward and backward reaction rate of the above reaction (R_+ and R_-, respectively, in mol/m^2/s) can be described as

$$R_+ = k'_+ \quad (2)$$

$$\begin{aligned} R_- &= k'_- \times \mathrm{Q}^n \\ &= k'_- \left(\frac{a^3_{Mg^{2+}}\ a^4_{SiO_2(aq)}}{a^6_{H^+}} \right)^n \end{aligned} \quad (3)$$

where k'_+ and k'_- are rate coefficients, and n is some positive constant expressing the dependence of the rate on the ion activity product, Q. The net reaction rate (R, mol/m^2/s) can be expressed as

$$\begin{aligned} R &= R_+ - R_- \\ &= k'_+ - k'_- \times \mathrm{Q}^n \end{aligned} \quad (4)$$

The relationship of the rate coefficients k'_+ and k'_- can be derived from the PDB theory that states that forward and backward rate are equal at equilibrium:

$$R_+ - R_- = k'_+ - k'_- \times \mathrm{Q}^n = 0 \tag{5}$$

which may be simplified to:

$$k'_+ = k'_- \times \mathrm{Q}^n \ . \tag{6}$$

By definition, at equilibrium, $Q = K_{eq}$, such that:

$$k'_+ / k'_- = (K_{eq})^n \tag{7}$$

Substituting Equation (7) into Equation (4) and combining with the definition of the saturation state (i.e., $\Omega = \mathrm{Q}/K_{eq}$) yields:

$$\begin{aligned} R &= R_+ - R_- \\ &= k'_+ - k'_- \, \mathrm{Q}^n \\ &= k'_- (K_{eq})^n (1 - \Omega^n) \end{aligned} \tag{8}$$

which is functionally the same as:

$$R = -k'_- (K_{eq})^n (\Omega^n - 1) \ , \tag{9}$$

which, in turn, compares favorably with the rate law employed by Arizaleta et al. (2020):

$$R = k(\Omega - 1)^n \ , \tag{10}$$

(where k is their empirically derived rate constant) especially at $\Omega >> 1$, where both $(\Omega^n - 1)$ and $(\Omega - 1)^n$ simplify to Ω^n. Also, compared with the derivation process of the TST rate law generated by Rimstidt and Barnes (1980), our reverse reaction rate (equation 3) as a function of the ion activity product involves a power n instead of a linear relationship. The power n is typically related to structural defects on the mineral surface (Lasaga, 2014). Equations 8-10 are expressions of the net TST rate law $r = k \cdot f(\Omega)$. This derivation demonstrates that combining Equations 4 and 7 is the key to the derivation of the overall TST rate law (Equations 8-10), which implicitly assumes that PDB applies not only at equilibrium but also at any degree of saturation. In other words, to derive the version of the TST rate law that is generally applicable to all saturation states, we must apply a relationship (Equation 7) that is derived from a specific saturation state (equilibrium). To validate the PDB and test its range of applicability, it is thus

necessary to assess the forward and backward rates at equilibrium and compare the forward or backward rate constants at different saturation states.

In this study, a non-traditional isotopic tracer (^{29}Si) was used to test the PDB and its applicability to the derivation of the TST rate law describing the growth of amorphous Mg-phyllosilicate. Enriched ^{29}Si was used to endow Mg-phyllosilicate-supersaturated experimental solutions with atypical isotopic compositions, and these solutions were reacted with the Mg-silicate substrates (amorphous Mg-silicate and crystalline Mg-silicate (talc)) with normal (i.e., bulk abundance) isotopic composition. Time-series measurements of the changes in the abundance ratios of Si isotopes and total Si concentrations in fluids sampled from these experiments allow simultaneous determination of the dissolution and precipitation rates of the Mg-silicate gel. The results suggest that the PDB, and hence the TST rate model, is applicable to amorphous Mg-phyllosilicate-water reactions.

2. Methods

2.1 Experimental design

Two sets of experiments are conducted in this study (Table 2). Due to the involvement of two types of substrates in our experiment (amorphous Mg-silicate and crystalline talc) and the commercial availability of crystalline talc, the first set of experiments is to synthesize the amorphous Mg-silicate (referred to as precipitation experiments). The second set of experiments is to interact the substrates with a ^{29}Si-doped supersaturated solution to test the PDB and its applicability.

Amorphous Mg-phyllosilicate was synthesized at room temperature in a series of experiments using batch reactors containing 2 mmol/kg SiO_2 (the total Si species in the solution), 5 mmol/kg Mg with pH = 10 at room temperature (21.5 ± 0.6 °C). This initial solution composition can be found in some natural lakes (cf. Chase et al., 2021), which was designed to be above the critical supersaturation for homogenous nucleation of Mg-silicates

and to precipitate an amorphous, kerolite-like phase (Tosca and Masterson, 2014; Chase et al., 2021). Because the initial pH (~10) is above the pK (~9.86) for silicic acid at ambient temperature, the solubility of amorphous silica is ~3 times higher than that at low pH (~6.5 mmol/kg at pH=10.1 (Tutolo and Tosca, 2018) compared to ~1.8 mmol/kg at pH=7 (Gunnarsson and Arnórsson, 2000)), preventing the precipitation of amorphous silica. Target Mg concentrations were achieved in all experiments by adding appropriate quantities of a 1 M $MgCl_2$ solution prepared by dissolving American Chemical Society (ACS) reagent-grade magnesium chloride hexahydrate ($MgCl_2 \cdot 6H_2O$) in deionized (18.2 MΩ) water. The 1 M $MgCl_2$ solution was diluted with deionized water 3-5 times and then slowly added to the experimental solution to prevent immediate precipitation. The source of silica used in the precipitation experiments was Baker Analyzed® sodium metasilicate nonahydrate ($Na_2SiO_3 \cdot 9H_2O$) that has a natural abundance of ^{28}Si (0.9223), ^{29}Si (0.0468), and ^{30}Si (0.0309), where the value in parentheses is the fraction of that isotope. This $Na_2SiO_3 \cdot 9H_2O$ was dissolved in deionized water in bottles and then adjusted pH to 10 by adding 1 M HCl or NaOH solution. The solution was then allowed to equilibrate with air for >24 hours, after which time pH was re-adjusted to the desired value. After nearly a week, the precipitates were acquired by passing the experimental solution through a 0.22 μm Durapore® (Polyvinylidene fluoride, PVDF) filter, rinsed with deionized water to remove any remaining dissolved components, and then dried at 60°C for 3-5 days. An additional precipitation experiment was duplicated without SiO_2 addition to evaluate the potential for brucite precipitation at these conditions.

It is important to note that the Si isotope composition of the Mg-silicate gel may differ slightly from natural composition due to isotopic fractionation during precipitation. While it would be vital to quantify these fractionation effects if we were attempting to quantify theisotopic fractionation during mineral precipitation, any reasonable amount of precipitation-induced fractionation would have a negligible effect on the determination of reaction rates. As

demonstrated below (Section 3.3), even when fractionation factors are as high as 1.005, the maximum errors on the determination of the rate are generally less than 0.5%, well within the uncertainties of the rate determinations.

PDB validation experiments (referred to as PDB experiments below) were performed at room temperature (Expt. IJ) and 65°C (Expt. IH and IG), which were chosen to be representative of the temperatures of early diagenesis and burial, respectively. Experiment IJ was performed by reacting the amorphous Mg-phyllosilicates synthesized in the precipitation experiments with pH = 9 solutions containing ~2 mmol/kg $^{29}SiO_2$ and ~4.5 mmol/kg Mg at room temperature; Expts. IH and IG were performed by reacting the amorphous Mg-phyllosilicates (Expt IH) and crystalline talc (Expt. IG) with pH = 8.5 solutions containing ~4.5 mmol/kg $^{29}SiO_2$ and ~0.5 mmol/kg Mg at 65°C. The pH was buffered using boric acid (0.05 M $B(OH)_3$) to control pH (Arizaleta et al., 2020). The initial saturation state of the solutions here (Table3) is several orders of magnitude supersaturated with respect to crystalline Mg-silicate (talc and sepiolite), slightly above the effective solubility of Mg-silicate gel, undersaturated with respect to brucite, and undersaturated with respect to amorphous silica (except Expt. IH which is close to the solubility of amorphous silica). The SiO_2 source used in the PDB experimental solutions was obtained from IsoFlex USA (San Francisco, California) as a ≥99.69% ^{29}Si-enriched oxide powder with the isotopic composition: ^{28}Si (0.0004), ^{29}Si (0.999), and ^{30}Si (0.0006), where the number in parentheses refers to the fraction of the isotope. It is worth emphasizing that the isotopic composition of the amorphous Mg-phyllosilicate and the talc substrates is rich in ^{28}Si and relatively poor in ^{29}Si, while the solution used here is rich in ^{29}Si and relatively poor in ^{28}Si. In this way, the interaction between the substrates and the solution can be precisely monitored by measuring the change of the fraction ^{29}Si in the solution.

The PDB experiments were conducted using a series of 0.6 mL microcentrifuge tubes containing a pre-weighed quantity of solid material. In Expt. IJ, each microcentrifuge tube

contained 0.04 g of amorphous Mg-silicate; in Expt. IH, each tube contained 0.02 g of amorphous Mg-silicate; and in Expt. IG, each tube contained 0.03 g of talc. The ^{29}Si solutions for room temperature (Expt. IJ) and 65°C (Expts. IH and IG) experiments were made separately by dissolving the $^{29}SiO_2$ powder in deionized (18.2 MΩ) water with pH > 10 and heating it at 65°C in the oven for over 24 hours (Tutolo et al., 2018). Boric acid (0.05 M) and 1 M HCl or NaOH solution was used to adjust and buffer pH at desired values. The ^{29}Si solution prepared for the 65°C experiments was re-heated for at least 48 hours to achieve near amorphous silica equilibrium concentration, while the ^{29}Si solution prepared for room temperature experiments was left standing at room temperature for at least 48 hours. Subsequently, the desired Mg concentration was achieved by adding 0.05 M $MgCl_2$ solution that was diluted from the 1M $MgCl_2$ solution into the ^{29}Si solutions. Finally, 0.6 g solution of these solutions was injected into each of the prepared microcentrifuge tubes via 0.22 μm Durapore® PVDF syringe filters. These microcentrifuge tubes then were shaken by hand to promote the contact of the solids and the solutions. The microcentrifuge tubes for Expt. IH and IG were quickly put into a pre-heated (65°C) Thermo Scientific™ Precision™ circulating water bath, with manufacturer specified temperature uniformity of ±0.05°C. The minute size of the microcentrifuge tubes in relation to the size of the water bath ensured rapid thermal equilibration.

Across all PDB experiments, reactions in the individual microcentrifuge tubes were terminated at specified times by removing the liquid from the tube via a needle-tipped syringe, filtering the solution through a 0.22 μm Durapore® PVDF syringe filter, and then processing it for analysis as discussed below (Chase et al., 2021). In this way, each experiment is truly a combination of several individual, sequentially sacrificed micro-reactors (microcentrifuge tubes). Combined with analysis of the starting solution, two adjacent samples allow determining 2 rates (one dissolution rate and one precipitation rate) when using both ^{28}Si and ^{29}Si. Since the micro-reactors are entirely isolated from one another over the course of each

experiment, consistency in trends observed over the course of the experiments demonstrates repeatability of the results.

2.2 Fluid analysis

The pH of the fluid samples was measured at room temperature on an aliquot of filtered solution using a Thermo Scientific™ PerpHecT™ Orion™ ROSS™ combination micro-electrode. The remaining sample was then diluted with 1 M HCl to prevent precipitation during storage. The Si concentration in the precipitation experiments and the Mg and Na concentration in both precipitation and PDB experiments were measured by Varian 725-ES Inductively Coupled Plasma Optical Emission Spectrophotometer (ICP-OES) with typical uncertainties better than ± 5.0%. Isotopic compositions (^{28}Si and ^{29}Si concentration) of the solutions acquired from the PDB experiments were measured by Thermo Scientific iCAP Triple Quadrupole (TQ) ICP-MS following calibration method and analysis procedures described by Zhang et al. (2020). Specifically, Zhang et al. (2020) measured ^{28}Si and ^{29}Si concentrations using the calibration curve method and calculated ^{30}Si based on a known ratio of ^{30}Si / ^{28}Si = 0.0336 due to the low concentration, and the calibration curve was established using the calibration standard solution. A series of the mixing samples with known ^{28}Si and ^{29}Si concentrations (Table S1), prepared by mixing 2.90 ppm ^{29}Si stock solution and 2.81ppm Si ICP standard in differenct ratios, have been measured to verify this calibration curve method. The highly linear calibration curves of ^{28}Si and ^{29}Si (Fig.S1) coupled with the significant agreement of the fraction of ^{29}Si between the measured and the expected (Fig.S2) demonstrate that the calibration curve method is capable of producing reliable Si isotope ratio within certain uncertainty. The uncertainty (RSDs) of ^{28}Si and ^{29}Si concentrations measured in our study is determined to be better than ± 2.5%. Precision of this magnitude is quite common in kinetics studies. For example, in the study of albite dissolution (Zhang et al., 2020) and kaolinite dissolution (Gong et al., 2019), the RSDs of ^{28}Si and ^{29}Si concentrations obtained from Q-ICP-MS were reported to be generally below

3%.

2.3 Solid analysis

Amorphous Mg-phyllosilicates collected from precipitation experiments were analyzed at the University of Calgary using Fourier transform infrared spectroscopy (FTIR), x-ray diffraction (XRD), and Raman spectroscopy. FTIR spectra were obtained in transmission mode over the wave number range from 400 cm^{-1} to 4000 cm^{-1} on optically translucent disks prepared by mixing the precipitated material with dried KBr powder. XRD analyses were performed using a Rigaku Multiflex X-ray diffractometer with a Cu Kα X-ray source. Raman spectra were obtained using a Horiba XploRA PLUS Raman microscope operated with a 532 nm Diode-Pumped Solid-State laser. In addition, the crystalline talc used in the PDB experiments was analyzed at the University of Oxford via powder X-ray diffraction using a Panalytical Empyrean Pro powder X-ray diffractometer outfitted with a Co X-ray source to confirm purity (Fig. S3). Finally, Brunauer–Emmett–Teller (Brunauer et al., 1938) surface areas of the amorphous Mg-silicate and the crystalline talc were measured using 5-point N_2 sorption method with a ChemBET 3000 instrument to be 1.83 m^2/g for talc and 365 m^2/g for the amorphous Mg-phyllosilicate.

Given the fact that structural changes of the Mg-silicates gels over the timescales of our PDB experiments are expected to be negligible (Tosca et al., 2011; Chase et al., 2021), only FTIR analysis was conducted on the Mg-phyllosilicate collected after the PDB experiments at 65℃, where the most detectable changes would reasonably be expected. The change of the isotopic composition of the amorphous Mg-silicate itself after PDB experiments was therefore not analyzed, since it is also expected to be negligible, as demonstrated by the following calculation: Assuming the amorphous substrates and the new precipitates have a talc-like ($Mg_3Si_4O_{10}(OH)_2$) stoichiometry, the 0.04 g of amorphous Mg-silicate in Expt. IJ corresponds to ~9.31 nmol ^{29}Si (0.04 g / 201 g·mol × 0.0468), and the ^{29}Si incorporated into the solid is

~0.96 nmol (see section 3.2 for the depletion of ^{29}Si in Expt. IJ, Δ^{29}Si (mmol/kg)=1.9 - 0.3 = 1.6, the mass of the solution is 0.6 g). Therefore, only ~1% change in the ^{29}Si composition of the solids would be expected for Expt. IJ, which is well within the uncertainty of the ICP-MS techniques we employ (Section 2.2.1). Similarly, it is hard to unambiguously analyze the composition and crystallinity of new precipitates on the substrates in the PDB experiments by using the above techniques due to the small amount and the subtle difference between the different phases of Mg-silicate gel (Tosca and Masterson, 2014; Arizaleta et al., 2020; Chase et al., 2021). Taking Expt. IJ as an example (0.04 g gel substrates), the amount of "new" precipitates can be calculated by the net reaction rates to be ~0.12 mg, which would suggest that only ~3% of the solids after the Expt. IJ were precipitated during the experiments.

2.4 Calculation techniques

2.4.1 Rate calculation with no fractionation

The use of non-traditional isotopes to trace reaction paths has been reported variously as the "isotope doping method" (Beck et al., 1992; Liu et al., 2016; Gong et al., 2019), "isotope attenuation method" (Berndt and Seyfried, 1999) , and "isotope ratio method" (Gruber et al., 2013). Assuming the fractionation during the reaction is negligible (which is reasonable based on the extremely different Si isotopic compositions of our fluids and solids), the reaction can be simply considered as a coupled dissolution and precipitation processes. Thus, the mass balance of ^{28}Si and ^{29}Si in the solution, the average dissolution rate R_{dis} and precipitation rate R_{pre} between two adjacent samples in the batch system can be expressed as follows:

$$\frac{d^{28}si}{dt} = r_{dis}\left(\frac{^{28}si}{total_{si}}\right)_{dis} - r_{pre}\left(\frac{^{28}si}{total_{si}}\right)_{\bar{t}} \quad (11)$$

$$\frac{d^{29}si}{dt} = r_{dis}\left(\frac{^{29}si}{total_{si}}\right)_{dis} - r_{pre}\left(\frac{^{29}si}{total_{si}}\right)_{\bar{t}} \quad (12)$$

$$R_{dis} = \frac{r_{dis}}{v \cdot S} \cdot m \quad (13)$$

$$R_{pre} = \frac{r_{pre}}{v \cdot S} \cdot m \quad (14)$$

where the subscript dis refers to the substrates, in which the isotope composition is natural and presumably remains unchanged. The subscript $\bar{t}$ refers to the solution at the middle time between two samples, in which the isotopes are changing with time due to the dissolution and precipitation. The variables r_{dis} and r_{pre} represent the rates of dissolution and precipitation normalized to the solution mass (mol/kg/s), while R_{dis} and R_{pre} denotes the dissolution and precipitation rate (mol/m^2/s) normalized to the surface of solids (S, m^2) that is assumed to be constant. The variable m represents the solution mass in the reactor (kg) and υ is the stoichiometric coefficient of Si of the reactants and products of the reactions, in which talc mineral formula ($Mg_3Si_4O_{10}(OH)_2$) is used both for reactants and products according to the characteristics of synthesized material (see section 3.1).

Rearranging the above equations gives

$$R_{dis} = \frac{m}{\upsilon \cdot S} \cdot \frac{\frac{d^{28}si}{dt} - \frac{d^{29}si}{dt} \cdot \left(\frac{^{28}si}{^{29}si}\right)_{\bar{t}}}{\left(\frac{^{28}si}{^{total}si}\right)_{dis} - \left(\frac{^{29}si}{^{total}si}\right)_{dis} \cdot \left(\frac{^{28}si}{^{29}si}\right)_{\bar{t}}} \tag{15}$$

$$R_{pre} = \frac{m}{\upsilon \cdot S} \cdot \frac{\frac{d^{28}si}{dt} - \frac{d^{29}si}{dt} \cdot \left(\frac{^{28}si}{^{29}si}\right)_{dis}}{\left(\frac{^{29}si}{^{total}si}\right)_{\bar{t}} \cdot \left(\frac{^{28}si}{^{29}si}\right)_{dis} - \left(\frac{^{28}si}{^{total}si}\right)_{\bar{t}}} \tag{16}$$

2.4.2 Rate calculation with isotopic fractionation

Although the rate determined by isotopic techniques assuming no fractionation has been proven reliable in feldspar dissolution experiments (Skulan et al., 2002; Gruber et al., 2013; Zhu et al., 2016), the reliability seems to depend not only on the true dissolution and precipitation rate of the reaction but also the duration of the experiment, especially in batch reactors. Since the assumption of no or negligible fractionation may be wrong (De La Rocha et al., 2000; Brantley et al., 2004; Wiederhold et al., 2006) and the fractionation effects in the amorphous Mg-silicate system have not yet been tested, we simulate the effects of the kinetic fractionation in our experiments following the method presented by Gruber et al (2013).

The fractionation factor of dissolution can be defined as:

$$\alpha_d = \frac{(\frac{d^{28}si/dt}{d^{29}si/dt})_{dis}}{(\frac{^{28}si}{^{29}si})_{dis}} \quad (17)$$

where $d^i si/dt$ denotes the dissolution rate of isotope i released from the surface of the solid (mol/kg/s), while the subscript dis refers to the solid (gel in this section). If no fractionation happens during dissolution, the ratio of ^{28}Si to ^{29}Si released should equal the ^{28}Si/^{29}Si of the solid. Similarly, the fractionation factor for precipitation can be described as:

$$\alpha_p = \frac{(\frac{d^{29}si/dt}{d^{28}si/dt})_{pre}}{(\frac{^{29}si}{^{28}si})_{\bar{t}}} \quad (18)$$

where $d^i si/dt$ denotes the incorporation rate of isotope i into the surface of the new precipitated phase (mol/kg/s), while the subscript pre refers to the new precipitated phase. If no fractionation happens during precipitation, the ratio of ^{29}Si to ^{28}Si incorporated into the new precipitates should equal the ^{29}Si/^{28}Si of the solution. Mathematically, the fractionation effect can be described as an isotopic exchange reaction, and a faster release or incorporation of one isotope must cause slower release or incorporation of another isotope. However, the direction and extent of the Si isotope fractionation during Mg-silicate gel formation and dissolution have not yet been experimentally constrained. The following calculations of the Si fractionation is based on the following assumptions: 1) atomic bonds involving the lighter isotopes have higher vibrational frequencies and tend to break first, and the ordered phase thus tends to accumulate heavier isotope; 2) the Si fractionation effects in the processes of precipitation and dissolution will strengthen each other, rather than weaken each other, resulting in greater errors. Assuming preferential release of ^{28}Si and preferential incorporation of ^{29}Si in the reaction, the mass balance on the surface of dissolved solids in the batch system can be described as:

$$(\frac{d^{28}si}{dt})_{dis} = r_{dt} \cdot \left(\frac{^{28}si}{^{total}si}\right)_{dis} + R_{exd} \quad (19)$$

$$(\frac{d^{29}si}{dt})_{dis} = r_{dt} \cdot \left(\frac{^{29}si}{total_{si}}\right)_{dis} - R_{exd} \quad (20)$$

where r_{dt} denotes the true dissolution rate (mol/kg/s) after taking account of the preferential release rate of ^{28}Si (R_{exd}, mol/kg/s). Substituting equation (19) and (20) into (17) gives:

$$R_{exd} = \frac{\alpha_d \cdot (\frac{28si}{29si})_{dis} \cdot r_{pt} \cdot \left(\frac{^{29}si}{total_{si}}\right)_{dis} - r_{dt} \cdot \left(\frac{^{28}si}{total_{si}}\right)_{dis}}{1 + \alpha_d \cdot \left(\frac{28si}{29si}\right)_{dis}} \quad (21)$$

Similarly, the mass balance on the surface of the new precipitates can be described as:

$$(\frac{d^{28}si}{dt})_{pre} = r_{pt} \cdot \left(\frac{^{28}si}{total_{si}}\right)_{\bar{t}} - R_{exp} \quad (22)$$

$$(\frac{d^{29}si}{dt})_{pre} = r_{pt} \cdot \left(\frac{^{29}si}{total_{si}}\right)_{\bar{t}} - R_{exp} \quad (23)$$

where r_{pt} denotes the true precipitation rate (mol/kg/s) after taking account of the preferential incorporation rate of ^{29}Si (R_{exp}, mol/kg/s). Substituting equation (22) and (23) into (18) gives:

$$R_{exp} = \frac{\alpha_p \cdot \left(\frac{29si}{29si}\right)_{\bar{t}} \cdot r_{pt} \cdot \left(\frac{^{28}si}{total_{si}}\right)_{\bar{t}} - r_{pt}\left(\frac{^{29}si}{total_{si}}\right)_{\bar{t}}}{1 + \alpha_p \cdot (\frac{29si}{29si})_{\bar{t}}} \quad (24)$$

The mass balance of the batch experiments that assumes more ^{28}Si dissolved from the surface of the solid and more ^{29}Si incorporated on the new precipitates can be described as following:

$$\frac{d^{28}si}{dt} = r_{dt}\left(\frac{^{28}si}{total_{si}}\right)_{dis} - r_{pt}\left(\frac{^{28}si}{total_{si}}\right)_{\bar{t}} + R_{exd} + R_{exp} \quad (25)$$

$$\frac{d^{29}si}{dt} = r_{dt}\left(\frac{^{29}si}{total_{si}}\right)_{dis} - r_{pt}\left(\frac{^{29}si}{total_{si}}\right)_{\bar{t}} - R_{exd} - R_{exp} \quad (26)$$

$$R_{dt} = \frac{r_{dt}}{v \cdot S} \cdot m \quad (27)$$

$$R_{pt} = \frac{r_{pt}}{v \cdot S} \cdot m \quad (28)$$

where R_{dt} and R_{pt} denotes the true dissolution and precipitation rate (mol/m^2/s) that excludes

the effects of fractionation. By assigning specific values to fractionation factors (α_d, α_p) and combining equation (21), (24), (25), and (26), the r_{dt} and r_{pt} can be calculated and then R_{dt} and R_{pt} can be calculated via Equation (27) and (28). The effects of fractionation on the calculated dissolution and precipitation rates can be evaluated by

$$error_{dis} = \frac{R_{dis} - R_{dt}}{R_{dis}} \tag{29}$$

and

$$error_{pre} = \frac{R_{pre} - R_{pt}}{R_{pre}}, \tag{30}$$

where $error_{dis}$ and $error_{pre}$ represent the relative error on the calculation of the dissolution and precipitation rates, respectively.

2.4.3 Geochemical calculations

The Geochemist's Workbench v. 12.0.5 (Bethke et al., 2018) employing the custom database presented by Tutolo and Tosca (2018) was used to calculate ion activities, mineral saturation states, and the *in situ* pH for the 65°C experiments. Activity coefficients of charged species were calculated using the extended ''B-dot'' Debye-Hückel equation (Helgeson, 1969). The composition of the measured solution was used to calculate the ionic activity product (Q) and saturation state (Ω) of minerals. The saturation state (Ω) is calculated as (Q/K_{eq}), where Q is calculated from the activity derived from the concentration determined in the solution, and K_{eq} represents the solubility product of the mineral of interest.

2.4.4 Error propagation

Gaussian error propagation techniques (Barrante, 2016) were used to estimate the uncertainty in some calculated parameters (e.g. Si concentration) and reaction rates (e.g. precipitation rates); the technique employed is consistent with the error propagation methods presented by Rimstidt (Rimstidt, 2014). This method can be described as:

$$\delta f = \sqrt{\sum_i (\frac{\partial f}{\partial x_i})^2 * (\delta\, x_i)^2} \tag{31}$$

where δf is the error of the calculated parameters, δx_i is the error of the measured elements (^{28}Si, ^{29}Si, and Mg) or the intermediate values produced during the calculation. The uncertainties on the ionic activity products (Q) are conservatively assumed to have a value of ±0.5 log units (Arizaleta et al., 2020).

3. Results

3.1 Precipitation experiments

The Mg/Si ratio of the precipitates can be inferred from the depletion of the Mg and Si in solution over the course of the precipitation experiment. The depletion of Mg and Si shows a linear trend and the value of the Mg/Si depletion is 0.63 ± 0.28 to 0.70 ± 0.35 (Table S2, also reported in Chase et al. (2021)) which is lower than the Mg/Si in the initial solution (~2.5) but consistent with the ideal ratio for talc/kerolite within error (0.75). This Mg/Si ratio is consistent with the trends observed in previous Mg-silicate precipitation experiments (compiled in Chase et al. (2021)). No precipitates were observed in the SiO_2-free experiment, indicating the brucite precipitation reaction is negligible. Moreover, the initial solution is just slightly supersaturated with brucite, and as Mg was being consumed by Mg-silicate formation in the precipitation experiments, pH dropped below ~9.3 (Table. S2), and the solution became undersaturated with respect to brucite.

FTIR spectra (Fig.1a) demonstrate that the precipitates are characterized by a 2:1 layered structure with tetrahedral Si sheet reflected at ~910 cm^{-1} and ~1024 cm^{-1} vibrations and with octahedral OH_3-Mg stretching at 3690 cm^{-1} (Hindshaw et al., 2019; Hindshaw et al., 2020). The vibration at 3430 cm^{-1} is related to the interlayer or surface-bound molecular H_2O (Tosca and Masterson, 2014). In particular, a lack of ~1200 cm^{-1} vibration diagnostic of inverted silica tetrahedra (Tosca and Masterson, 2014; Tutolo and Tosca, 2018) demonstrates the absence of a sepiolite-like or loughlinite-like phase in the precipitates, which is in clear contrast with the obvious absorption of sepiolite shown by Baldermann et al. (2018). The lack of vibrational

features at 800 cm^{-1} and 3720-3700 cm^{-1} excludes the presence of amorphous silica and brucite in the synthesized precipitates (Baldermann et al., 2018). Consistent with the FTIR spectra, the presence of peaks at ~1.5 Å, ~2.4 Å, ~3.6 Å, and ~4.0 Å in XRD patterns (Fig.1b) is consistent with a talc/kerolite-like precipitate (Tosca et al., 2011; Tosca and Masterson, 2014; Tutolo and Tosca, 2018; Chase et al., 2021). The broad peak and poorly resolvable *hkl* reflections indicate that the precipitates are poorly crystalline and lack stacking order between TOT sheets. Raman spectra of the synthesized particles are in excellent agreement with spectra acquired on crystalline talc from Murphy, North Carolina, USA (RRUFF ID: R050058) (Fig. 1c). Specifically, the strong bending of Si–O–Si bridges around 670 cm^{-1} (Reynard et al., 2015) is in direct correspondence to the standard sample. Even though the middle-frequency spectrum (250–650 cm^{-1}) is poorly resolvable, the slight bump is likely indicative of the lattice vibration involving Mg–O bonds and tetrahedral bending. Together, the depletion of Mg and Si in solution and the FTIR, XRD, and Raman measurements demonstrate that the precipitated material is a hydrated talc/kerolite-like phase with a poorly crystalline structure.

3.2 PDB validation experiments

The FTIR spectra of post-experiment samples show that the structural characteristics of the solids are virtually unchanged apart from a slight narrowing of the bands after the PDB experiments at 65°C (Fig.1a). Fluid chemistry, Si isotopic abundances, and reaction rates calculated from these data show consistent trends over the course of each of the PDB experiments (Table 3, Fig. 2). In Expt. IJ, the fraction of ^{28}Si in the fluid increases, and the fraction of ^{29}Si in the fluid decreases across the entire duration of the experiment (Fig. 2a). The Si, Mg, and Na concentrations decrease over the first 20 minutes and then slightly level off and stay roughly constant over 2 hours (Fig. 2b and table 3). The calculated rates of precipitation are slightly faster than the dissolution rates at the beginning of the experiments, but, as the reaction proceeds, the precipitation rate slows and approaches the dissolution rate within the

uncertainty (Fig.2c). Expt. IH behaves similarly with Expt. IJ in terms of the trend of the fraction of ^{28}Si, ^{29}Si, and Si concentrations (Fig.2d and 2e). Nevertheless, the Mg concentration increases in the first 10 minutes and then decreases, and the Na concentration decreases throughout the experiment (Fig.2e and table3). The precipitation and dissolution rates are faster than those measured in Expt. IJ but show a similar trend (Fig.2f). Expt. IG shows little change of the fraction of ^{28}Si and ^{29}Si (Fig.2g), suggesting limited talc dissolution. The concentration of Si and Mg (and Fig. 2i) decreases significantly, indicating significant net precipitation of Mg-silicate, while the Na concentration remains approximately constant throughout the reaction.

A fit of Equation (3) to the precipitation rates measured in Expt. IJ compares favorably to the heterogeneous growth rates reported at pH ~9 by Arizaleta et al. (2020) (Fig 3a). The collected rates effectively share the same rate function, and consequently the same rate constant. The heterogeneous growth rates (net reaction rates) reported by Arizaleta et al. (2020) were recalculated here using the stoichiometric coefficient of Si in talc (4) instead of their sepiolite (3.11) to remain consistent with our experiments (see Section 4.1 for further justification). The heterogeneous growth rates were also assumed to be equivalent to the unidirectional precipitation rates, which is justified by the results shown by Expt. IG where the net growth rates are virtually the same as the precipitation rates. Similarly, we have fit Equation (3) to the precipitation rates measured in Expt. IH and IG (Fig.3b). Even though the correlation is tenuous due to the limited number of measurements, the precipitation rates of Expt. IH coupled with the same dissolution rates appear to share the same rate function with the Expt. IG precipitation rates, for which the dissolution rates are negligible within measurement uncertainty.

3.3 The effects of Si isotope fractionation

Two conditions have been considered to assess the effects of Si isotope fractionation on our calculation of reaction rates. One only considers fractionation during precipitation and the

other considers fractionation during both precipitation and dissolution. Regardless of whether the precipitation fractionation coefficient in our model is 1.005, or the precipitation fractionation coefficient and the dissolution fractionation coefficient are both 1.005, the maximum error between the reaction rates calculated in experiment IJ and IG and the true reaction rates will not exceed 0.6% (Table 4). The results obtained by taking Expt. IG as an example and setting the fractionation coefficients as sequentially increasing from 1 to 1.005 in the above two scenarios are shown in Fig. 4. The results demonstrate that the errors on the precipitation rates (Fig 4a and 4c) and dissolution rates (Fig.4b and 4d) are less than 0.4%. In general, the error increases with the fractionation coefficient and time, but an abnormally high error has been calculated for the dissolution rates at 10-15 mins.

Our calculations suggest that fractionation during dissolution has a more limited effect than during precipitation (Table 3), which is consistent with the Mg isotope changes during magnesite dissolution and precipitation experiment conducted by Pearce et al. (2012). Although isotope fractionation effects may be more significant over timescales longer than our experiments, the overall effects of fractionation caused either by dissolution or precipitation processes at the given values are negligible in our experiments.

4. Discussion

4.1 PDB on amorphous Mg-silicates

Our results show that the ratios of the forward and backward rates of amorphous Mg-phyllosilicate-water reaction approach unity as solution saturation state approaches the apparent solubility (Fig.2c and 2f). The precipitation rates coupled with the same dissolution rates can be described using the same rate function with the precipitation rates coupled with negligible dissolution rates (Fig. 3), which suggests that the rate-limiting step of amorphous Mg-silicate precipitation remains unchanged across the degrees of supersaturation explored in Fig. 3 and is independent of the dissolution process at these conditions. The results thus suggest

that the Principle of Detailed Balance is applicable to amorphous Mg-phyllosilicate-water reaction, which, in turn, provides experimental evidence to justification the application of TST rate law on the growth of Mg-phyllosilicates (Arizaleta et al., 2020).

PDB theory states that at equilibrium, the forward and backward rates are equal, but, interestingly, our experiments demonstrate that forward and backward rates of amorphous Mg-silicate-water reaction exhibit the same values near the apparent solubility, i.e., the conditions under which they were started. Because the amorphous materials are, by definition, thermodynamically unstable and typically incompletely characterized, it is difficult to conclusively demonstrate equilibrium with respect to either these amorphous materials or crystalline Mg-phyllosilicates. Rather, measurements of fluid chemistry at the conclusion of homogenous nucleation/growth experiments are typically interpreted as the apparent solubility of the amorphous phase (Tosca et al., 2011), which can be explained according to kinetic theory of nucleation (Tutolo and Tosca, 2018; Jiang and Tosca, 2019).

Importantly, our experimental measurements of reaction rates at the apparent solubility of amorphous Mg-silicate provide vital insight into the dynamics of this process. Indeed, our measurements illustrate that the dissolution and precipitation rates are virtually equivalent when the saturation state approaches the apparent solubility, suggesting elevated reactivity of the Mg-phyllosilicate gels and a rapid approach to the quasi-equilibrium state of apparent solubility. Therefore, the concept of the apparent solubility of Mg-phyllosilicate not only corresponds to the critical supersaturation for homogeneous nucleation but also implies a metastable equilibrium between the amorphous material and the fluid. In other words, the apparent solubility also has a thermodynamic meaning, reflecting an equilibrium solubility control, but to a poorly-crystalline (amorphous) phase whose composition and structure may be evolving with time. However, it is worth emphasizing that this is the first time that the concept of quasi-equilibrium with respect to Mg-silicate gel has been demonstrated in this way,

i.e., mechanistically. Even though these measurements are in agreement with the value of apparent solubility of Mg-silicate gel at room temperature that has been documented in Lake Yoa (cf. Darragi and Tardy, 1987) and in experimental systems (cf. Tosca et al., 2011), further studies to observe coupled forward and backward reaction rates and dissolution rates near the apparent solubility of Mg-silicates with higher Si isotope precision and over longer experimental times will likely be required to confirm them.

To maintain consistency with our experimental measurements, we have re-normalized the rates from Arizaleta et al. (2020) to the stoichiometric coefficient of Si in talc (4) instead of 3.11, which, as noted by Arizaleta et al. (2020), is allowable within the uncertainties of their data (this results in rates ~ 29% higher, which is well within the uncertainties of their data, as they discuss). Nevertheless, we assess the impacts of using 4 rather than 3.11 and calculated the ion activity product (Q) for a phase of sepiolite stoichiometry (Fig. S4). Similar to the results presented in Fig. 3, these calculations demonstrate that the Arizaleta et al. (2020) data and our data can still be fitted with the same rate function, again suggesting that the measured rates adhere to the PDB theory.

4.2 Geological Implications

The quasi-equilibrium reflected by the relatively rapid dissolution and reprecipitation near the apparent solubility of amorphous Mg-phyllosilicate suggests that Si isotopic signatures can be rapidly and wholly reset during the earliest stages of sedimentation. The Si isotopic signatures acquired from homogeneous nucleation from supersaturated waters (e.g., alkaline lakes) may not be preserved as the precipitated phase undergoes further water-rock interaction. This Si isotopic re-setting would be consistent with similar processes observed for Mg in magnesite (Pearce et al., 2012), Ba in barite (Curti et al., 2010), and Fe in primary phyllosilicates (Kiczka et al., 2010). Particularly, some studies demonstrate a continuous exchange of isotopes in systems that are at chemical equilibrium (Mavromatis et al., 2016;

Stamm et al., 2019). For example, Mavromatis et al. (2016) demonstrated that isotopic dis-equilibrium of Ba in witherite ($BaCO_3$) can prevail in a system where chemical equilibrium in the system is reached, indicating a continuous exchange of Ba^{2+} between witherite and fluid when chemical equilibrium is attained. These results are in excellent agreement with our experiments and the PDB theory, indicating the chemical equilibrium is dynamic in a mineral-fluid system, and the understanding of the dynamic chemical equilibrium (including forward and backward process) can also allow the development of detailed models to explain the isotope fractionations (cf. (DePaolo, 2011)). However, the comparison between the amorphous Mg-phyllosilicate experiments and our experiments on crystalline talc suggests that, as the precipitated phase increases in crystallinity, its isotopic signature becomes increasingly difficult to reset.

In addition to affecting the preservation of isotopic signals, this quasi-equilibrium between supersaturated solutions and the amorphous Mg-phyllosilicate substrates may also affect the net heterogeneous growth rates during early diagenesis. Compared with crystalline talc, the amorphous Mg-phyllosilicates provide more abundant surface area for heterogeneous growth, but net growth rates on the amorphous substrate are considerably slower than those measured on mineral substrates (Table 3). The reduction in the net growth rates as the solution approaches the apparent solubility of the amorphous phase is consistent with the Mg-silicate growth experiments buffered by $KHCO_3$-K_2CO_3 conducted by Tutolo and Tosca (2018), in which the saturation state did not drop below the critical saturation state, but inconsistent with some the substrates-free experiments buffered by $NaHCO_3$-Na_2CO_3 in which the saturation state drops below the critical saturation state. As noted by Tutolo and Tosca (2018), it seems that elevated levels of Na^+ in solution, when accompanied by the presence of sufficient mineral substrates, can help to overcome the energetic barrier to facilitate the growth of Mg-silicate and continue to deplete the Si and Mg in the solution even below the critical supersaturation.

The observation of slower heterogeneous growth rates on amorphous substrates than on crystalline substrates also suggests that the depletion of Mg and Si in pore waters during early diagenesis is related to the evolution of crystallinity of the magnesium silicate. Interestingly, early-time data (0-10 mins) from Expt. IH indicate that the amorphous Mg-phyllosilicate released, rather than consumed, Mg, a process which was also observed in experiments run over a period of 356 days by Chase et al. (2021) at 60°C. In both sets of experiments, the coupled Mg release and Si depletion likely resulted from the evolution and crystallization of the amorphous starting materials, although, given the low water-to-rock ratios, neither experimental system would have yielded differing precipitate mineralogy (as confirmed by sequential XRD measurements presented by Chase et al. (2021)). If we assume that the crystallinity of the amorphous starting materials is ~0% and the crystallinity of final stable products (talc, in this case) is 100%, there will be a continuum of degrees of crystallinity between these two end members. Given that the quasi-equilibrium of amorphous Mg-silicate represents its apparent solubility at room temperature, the quasi-equilibrium solubility products of the intermediates must fall somewhere between the apparent solubility and the equilibrium solubility of talc, in a manner akin to the experimentally demonstrated variable solubility of kaolinites depending on their crystallinity (Nagy et al., 1991; Tutolo et al., 2014).

This refined understanding of the evolution of mineral solubility with crystallinity can help to inform a revised conceptual model for the heterogeneous growth of Mg-phyllosilicates during the early stages of sedimentation and burial. When the amorphous Mg-phyllosilicate nucleates and grows from solution, it reduces the free energy of the system to approach the metastable, quasi-equilibrium state representative of the apparent solubility. At this stage, net growth of Mg-phyllosilicates is halted, and the coexisting water remains at the apparent solubility (Darragi and Tardy, 1987). With the passage of time, occlusion of pore water from the overlying water column, and the accumulation of overlying sediments, the amorphous

materials will gradually dehydrate and increase in crystallinity, such that the still-supersaturated pore waters will promote heterogeneous growth of increasingly crystalline materials (Arizaleta et al., 2020). Eventually, the Mg-phyllosilicate will reach a steady-state degree of crystallinity that is only likely to change if environmental conditions change dramatically or after the passage of extended periods of geologic time. Ultimately, the rates of crystallization and heterogeneous growth are coupled, but further experimental and modeling work taking into account the results presented here, as well as those reported by Arizaleta et al. (2020) and Chase et al. (2021), will be required in order to refine our understanding of this process.

5. Future work

5.1 Insights into the Si isotope fractionation during Mg-phyllosilicate formation

The effects of kinetic Si isotope fractionation on the rate errors have been simulated through the above models based on the assumption of known direction and fractionation factors. Hindshaw et al. (2020) assessed the Mg isotopic fractionation during clay formation, and concluded that the direction of the incorporation of Mg isotopes is complicated and dependent on the specific conditions. However, the direction and extent of silicon isotope fractionation and the impact of temperature, pH, and the solution composition during the formation of clay minerals remain poorly constrained, potentially hindering the use of silicon isotopes as a paleo-environment proxy toconstrain global geochemical cycles. Therefore, the determination of the direction and amount of the fractionation of silicon isotopes during the formation of clay minerals is logically important to be one of the future works.

A series of experiments can be performed to assess the above issues. Specifically, Mg-silicate gel can be precipitated in batch reactors with different temperature and pH conditions. During this process, Si isotope measurements can be performed on digested solids and time series measurements of the precipitating solutions. Then, the isotopic fractionation defined as

the relative partitioning of the heavier and lighter isotopes between two coexisting phases can be determined. One potential challenge might be separating the silicon absorbed on the surface or existed in the interlayers (exchangeable) from the silicon incorporated into the tetrahedral structure.

Two types of isotopic fractionation processes are typically defined in the natural system, the "kinetic" and "equilibrium" fractionation (Tiwari et al., 2015). Kinetic fractionation is related to incomplete and one-way processes, in which no isotopic equilibrium is attained. Equilibrium fractionation is a special case of chemical equilibrium reaction in which there is no net reaction but isotopic exchange occurs. Pearce et al. (2012) determined the kinetically induced isotopic fluid-mineral fractionation during congruent magnesite dissolution and precipitation but suggested that the fractionation signature obtained from the far-from-equilibrium kinetic process would disappear as the backward reaction gains in importance. If that is the case in the amorphous Mg-silicate-water system, the equilibrium isotope fractionation, from the perspective of TST theory, can also be divided into two kinetic fractionation effects that compensate for each other. It is difficult to separate the equilibrium fractionation into two kinetic fractionation processes via any geochemical tracer. However, forward models might be able to decipher this isotope fractionation mechanism within TST theory at equilibrium.

5.2 Modeling the heterogeneous growth rates with evolving crystallinity

The heterogeneous growth rates will increase as the crystallinity of Mg-silicate substrates increase. However, the construction of an improved model of the heterogeneous growth of Mg-silicates during the early stages of sedimentation and burial brings up a few further questions. First, *Does the heterogeneous growth rate linearly increase with crystallinity?* Second, *what is the solubility of the Mg-silicates with different crystallinity*? Last, *what are the rates of the crystallization of Mg-silicates gel*?

Mg-silicate with different crystallinity can be synthesized by heating the Mg-silicate gel under high temperature for varying lengths of time, and the crystallinity can be determined by XRD measurements. Then, heterogeneous growth rate experiments with this different crystallized material as substrates can be performed. As to the second question, the solubility of these Mg-silicates can be determined by equilibrating them with a solution and then measuring the composition of the equilibrated solution. Although Murata et al. (2009) have determined the crystallization rates of Mg-silicates at high temperatures, it is unknown if the activation energy gained from the high-temperature range is applicable at the low-temperature range that is more realistic at the early burial state. Crystallization rates at low temperatures can be determined by putting Mg-silicate gel in the oven and then test the crystallinity change with time.

6. **Conclusion**

In this study, the Principle of Detailed Balance and its application to the interactions between Mg-phyllosilicate substrates (amorphous and crystalline Mg-silicate) and supersaturated solutions have been tested using the Si isotope doping method. The results show that: the forward and backward reaction of amorphous Mg-phyllosilicate-water reaction are approximately equal in solutions poised near the apparent Mg-phyllosilicate solubility; the rate-limiting step of the precipitation of Mg-silicate gel remains unchanged over the degrees of supersaturation that we have explored; and precipitation rates are independent of dissolution rates. Together, these results have verified the PDB and its applicability to the multi-component Mg-phyllosilicate system. To complement its previous explanation via kinetic theory of nucleation and growth, we have also shown that the apparent solubility of Mg-phyllosilicates can be explained in a thermodynamic sense, in that it represents a metastable equilibrium with respect the amorphous Mg-phyllosilicate. This quasi-equilibrium not only has the potential to

eliminate the isotopic signature acquired from the precipitating solution, but will also slow down net growth rates during diagenesis, since, as demonstrated by our experiments, the crystallinity of Mg-phyllosilicates is an important factor controlling the heterogeneous growth rates during diagenesis.

References

Aagaard P. and Helgeson H. C. (1982) Thermodynamic and kinetic constraints on reaction rates among minerals and aqueous solutions. I. Theoretical considerations. *Am. J. Sci.* **282**, 237–285.

Arizaleta M. L., Nightingale M. and Tutolo B. M. (2020) A rate law for sepiolite growth at ambient temperatures and its implications for early lacustrine diagenesis. *Geochim. Cosmochim. Acta* **288**, 301–315.

Baldermann A., Mavromatis V., Frick P. M. and Dietzel M. (2018) Effect of aqueous Si/Mg ratio and pH on the nucleation and growth of sepiolite at 25 °C. *Geochim. Cosmochim. Acta* **227**, 211–226.

Barrante J. R. (2016) *Applied Mathematics for Physical Chemistry*., Waveland Press, Inc., Long Grove, IL.

Beck J. W., Berndt M. E. and Seyfried W. E. (1992) Application of isotopic doping techniques to evaluation of reaction kinetics and fluid/mineral distribution coefficients: An experimental study of calcite at elevated temperatures and pressures. *Chem. Geol.* **97**, 125–144.

Berndt M. E. and Seyfried W. E. (1999) Rates of aragonite conversion to calcite in dilute aqueous fluids at 50 to 100°C: Experimental calibration using Ca-isotope attenuation. *Geochim. Cosmochim. Acta* **63**, 373–381.

Bethke C. M., Farrell B. and Yeakel S. (2018) *The Geochemist's Workbench® Release 12.0 - Reaction Modeling Guide*., Aqueous Solutions, LLC.

Brady P. V. (1992) Surface complexation and mineral growth: Sepiolite. *Water-rock Interact. Proc. 7th Int. Symp. Water-Rock Interact.*, 85–88.

Brantley S. L., Liermann L. J., Guynn R. L., Anbar A., Icopini G. A. and Barling J. (2004) Fe isotopic fractionation during mineral dissolution with and without bacteria. *Geochim.*

Cosmochim. Acta **68**, 3189–3204.

Brunauer S., Emmett P. H. and Teller E. (1938) Adsorption of gases in multimolecular layers. *J. Am. Chem. Soc.* **60**, 309–319.

Burch T., Nagy K. and Lasaga A. (1993) Free energy dependence of albite dissolution kinetics at 80 °C. *Chem. Geol.* **105**, 137–162.

Chase J. E., Arizaleta M. L. and Tutolo B. M. (2021) A series of data-driven hypotheses for inferring biogeochemical conditions in alkaline lakes and their deposits based on the behavior of Mg and SiO_2. *Minerals* **11**, 106.

Curti E., Fujiwara K., Iijima K., Tits J., Cuesta C., Kitamura A., Glaus M. A. and Müller W. (2010) Radium uptake during barite recrystallization at 23±2°C as a function of solution composition: An experimental ^{133}Ba and ^{226}Ra tracer study. *Geochim. Cosmochim. Acta* **74**, 3553–3570.

Darragi F. and Tardy Y. (1987) Authigenic trioctahedral smectites controlling pH, alkalinity, silica and magnesium concentrations in alkaline lakes. *Chem. Geol.* **63**, 59–72.

Deer W. A. (1966) *An introduction to the rock-forming minerals*.,

DePaolo D. J. (2011) Surface kinetic model for isotopic and trace element fractionation during precipitation of calcite from aqueous solutions. *Geochim. Cosmochim. Acta* **75**, 1039–1056.

Earle S. (2019) *Physical geology*., BCcampus Open Education.

Gong L., Rimstidt J. D., Zhang Y., Chen K. and Zhu C. (2019) Unidirectional kaolinite dissolution rates at near-equilibrium and near-neutral pH conditions. *Appl. Clay Sci.* **182**, 1–8.

Gruber C., Harpaz L., Zhu C., Bullen T. D. and Ganor J. (2013) A new approach for measuring dissolution rates of silicate minerals by using silicon isotopes. *Geochim. Cosmochim. Acta* **104**, 261–280.

Gunnarsson I. and Arnórsson S. (2000) Amorphous silica solubility and the thermodynamic properties of H4SiO 4 in the range of 0 to 350 C at Psat. *Geochim. Cosmochim. Acta* **64**, 2295–2307.

Gunnarsson I., Arnórsson S. and Jakobsson S. (2002) *Magnesium-silicate scales in geothermal utilization. An experimental study*.,

Gunnarsson I., Arnórsson S. and Jakobsson S. (2005) Precipitation of poorly crystalline antigorite under hydrothermal conditions. *Geochim. Cosmochim. Acta* **69**, 2813–2828.

Helgeson H. C. (1969) Thermodynamics of hydrothermal systems at elevated temperatures and pressures. *Am. J. Sci.* **267**, 729–804.

Hellmann R. and Tisserand D. (2006) Dissolution kinetics as a function of the Gibbs free energy of reaction: An experimental study based on albite feldspar. *Geochim. Cosmochim. Acta* **70**, 364–383.

Hindshaw R. S., Tosca R., Goût T. L., Farnan I., Tosca N. J. and Tipper E. T. (2019) Experimental constraints on Li isotope fractionation during clay formation. *Geochim. Cosmochim. Acta* **250**, 219–237.

Hindshaw R. S., Tosca R., Tosca N. J. and Tipper E. T. (2020) Experimental constraints on Mg isotope fractionation during clay formation: Implications for the global biogeochemical cycle of Mg. *Earth Planet. Sci. Lett.* **531**, 115980.

Jiang C. Z. and Tosca N. J. (2019) Fe(II)-carbonate precipitation kinetics and the chemistry of anoxic ferruginous seawater. *Earth Planet. Sci. Lett.* **506**, 231–242.

Kent D. B. and Kastner M. (1985) Mg^{2+} removal in the system Mg^{2+}-amorphous SiO_2-H_2O by adsorption and Mg-hydroxysilicate precipitation. *Geochim. Cosmochim. Acta* **49**, 1123–1136.

Kiczka M., Wiederhold J. G., Frommer J., Kraemer S. M., Bourdon B. and Kretzschmar R. (2010) Iron isotope fractionation during proton- and ligand-promoted dissolution of

primary phyllosilicates. *Geochim. Cosmochim. Acta* **74**, 3112–3128.

De La Rocha C. L., Brzezinski M. A. and Deniro M. J. (2000) A first look at the distribution of the stable isotopes of silicon in natural waters. *Geochim. Cosmochim. Acta* **64**, 2467–2477.

Lasaga A. C. (2014) *Kinetic theory in the earth sciences*., Princeton University Press, Princeton, New Jersey.

Lasaga Antonio C. (1981) Transition State Theory. In *Reviews in Mineralogy & Geochemistry v. 8: Kinetics of Geochemical Processes* (eds. A.C. Lasaga and R. J. Kirkpatrick).

Liu Z., Rimstidt J. D., Zhang Y., Yuan H. and Zhu C. (2016) A stable isotope doping method to test the range of applicability of detailed balance. *Geochemical Perspect. Lett.* **2**, 78–86.

Mavromatis V., van Zuilen K., Purgstaller B., Baldermann A., Nägler T. F. and Dietzel M. (2016) Barium isotope fractionation during witherite (BaCO3) dissolution, precipitation and at equilibrium. *Geochim. Cosmochim. Acta* **190**, 72–84.

Murata K., Chihara H., Koike C., Takakura T., Imai Y. and Tsuchiyama A. (2009) Crystallization experiments on amorphous magnesium silicate. I. estimation of the activation energy of enstatite crystallization. *Astrophys. J.* **697**, 836.

Nagy K., Blum A. and Lasaga A. C. (1991) Dissolution and Precipitation Kinetics of Kaolinite at 80 C and pH 3 the Dependence on Solution Saturation. *Am. J. Sci.* **291**, 649–686.

Pearce C. R., Saldi G. D., Schott J. and Oelkers E. H. (2012) Isotopic fractionation during congruent dissolution, precipitation and at equilibrium: Evidence from Mg isotopes. *Geochim. Cosmochim. Acta* **92**, 170–183.

Pozo M. and Galán E. (2015) Magnesian clay deposits: Mineralogy and origin. In *Magnesian*

Clays: Characterization, Origin and Applications pp. 175–228.

Reynard B., Bezacier L. and Caracas R. (2015) Serpentines, talc, chlorites, and their high-pressure phase transitions: a Raman spectroscopic study. *Phys. Chem. Miner.* **42**, 641–649.

Rimstidt J. D. (2014) *Geochemical rate models: an introduction to geochemical kinetics*., Cambridge University Press.

Rimstidt J. D. (1997) Quartz solubility at low temperatures. *Geochim. Cosmochim. Acta* **61**, 2553–2558.

Saldi G. D., Köhler S. J., Marty N. and Oelkers E. H. (2007) Dissolution rates of talc as a function of solution composition, pH and temperature. *Geochim. Cosmochim. Acta* **71**, 3446–3457.

Skulan J. L., Beard B. L. and Johnson C. M. (2002) Kinetic and equilibrium Fe isotope fractionation between aqueous Fe(III) and hematite. *Geochim. Cosmochim. Acta* **66**, 2995–3015.

Spinthaki A., Petratos G., Matheis J., Hater W. and Demadis K. D. (2018) The precipitation of "magnesium silicate" under geothermal stresses. Formation and characterization. *Geothermics* **74**, 172–180.

Stamm F. M., Zambardi T., Chmeleff J., Schott J., von Blanckenburg F. and Oelkers E. H. (2019) The experimental determination of equilibrium Si isotope fractionation factors among H4SiO4o, H3SiO4− and amorphous silica (SiO2· 0.32 H2O) at 25 and 75° C using the three-isotope method. *Geochim. Cosmochim. Acta* **255**, 49–68.

Tiwari M., Singh A. K. and Sinha D. K. (2015) *Stable Isotopes: Tools for Understanding Past Climatic Conditions and Their Applications in Chemostratigraphy*., Elsevier Inc. Available at: http://dx.doi.org/10.1016/B978-0-12-419968-2.00003-0.

Tosca N. J. (2015) Geochemical pathways to Mg-clay formation. *Magnesian Clays Charact.*

Orig. Appl. **2**, 283–329.

Tosca N. J. . and Masterson A. L. (2014) Chemical controls on incipient Mg-silicate crystallization at 25°C: Implications for early and late diagenesis. *Clay Miner.* **49**, 165–194.

Tosca N. J., Macdonald F. A., Strauss J. V., Johnston D. T. and Knoll A. H. (2011) Sedimentary talc in Neoproterozoic carbonate successions. *Earth Planet. Sci. Lett.* **306**, 11–22.

Tutolo B. M., Kong X. Z., Seyfried W. E. and Saar M. O. (2014) Internal consistency in aqueous geochemical data revisited: Applications to the aluminum system. *Geochim. Cosmochim. Acta* **133**, 216–234.

Tutolo B. M., Luhmann A. J., Tosca N. J. and Seyfried W. E. (2018) Serpentinization as a reactive transport process: The brucite silicification reaction. *Earth Planet. Sci. Lett.* **484**, 385–395.

Tutolo B. M. and Tosca N. J. (2018) Experimental examination of the Mg-silicate-carbonate system at ambient temperature: Implications for alkaline chemical sedimentation and lacustrine carbonate formation. *Geochim. Cosmochim. Acta* **225**, 80–101.

Wegscheider R. (1911) Über simultane Gleichgewichte und die Beziehungen zwischen Thermodynamik und Reactionskinetik homogener Systeme. *Monatshefte für Chemie und verwandte Teile anderer Wissenschaften* **32**, 849–906.

Wiederhold J. G., Kraemer S. M., Teutsch N., Borer P. M., Halliday A. N. and Kretzschmar R. (2006) Iron isotope fractionation during proton-promoted, ligand-controlled, and reductive dissolution of goethite. *Environ. Sci. Technol.* **40**, 3787–3793.

Wollast R., Mackenzie F. T. and Bricker O. P. (1968) Experimental Precipitation and Genesis of Sepiolite At Earth- Surface Conditions. *Am. Mineral.* **53**, 1645–1662.

Zhang Y., Gong L., Chen K., Burkhart J., Yuan H. and Zhu C. (2020) A method for Si

isotope tracer kinetics experiments: Using Q-ICP-MS to obtain 29Si/28Si ratios in aqueous solutions. *Chem. Geol.* **531**, 119337.

Zhu C., Donald Rimstidt J., Zhang Y., Kang J., Schott J. and Yuan H. (2020) Decoupling feldspar dissolution and precipitation rates at near-equilibrium with Si isotope tracers: Implications for modeling silicate weathering. *Geochim. Cosmochim. Acta* **271**, 132–153.

Zhu C., Liu Z., Zhang Y., Wang C., Scheafer A., Lu P., Zhang G., Georg R. B., Yuan H. lin and Rimstidt J. D. (2016) Measuring silicate mineral dissolution rates using Si isotope doping. *Chem. Geol.* **445**, 146–163.

Tables and Figures

Table 1: Lists of symbols and abbreviation

Symbols	Explanation
K_{eq}	Equilibrium constant
k^+	Forward rate constant
k^-	Backward rate constant
R_+	Forward reaction rate for the talc-water reaction (dissolution) in mol (talc) /m^2/s
R_-	Backward reaction rate for the talc-water reaction (precipitation) in mol (talc)/m^2/s
k'_+	The forward reaction rate constant for the dissolution of talc
k'_-	The backward reaction rate constant for the precipitation of talc
Q	Ion activity product
R	The net reaction rate for the talc-water reaction; $R = R_+ - R_-$
Ω	Saturation state
r_{dis}	Dissolution rate (mol/kg/s) of the Mg-silicate substrates normalized to the solution mass (m, kg)
r_{pre}	Precipitation rate (mol/kg/s) of Mg-silicate gel normalized to the solution mass (m, kg)
m	the solution mass (kg) in the batch reactor (microcentrifuge tube in our study)
R_{dis}	Dissolution rate (mol/m^2/s) of the Mg-silicate substrates normalized to the surface of the substrates (S, m^2)
R_{pre}	Precipitation rate (mol/m^2/s) of Mg-silicate gel normalized to the surface of the substrates (S, m^2)
R_{net}	The heterogeneous growth (net) rate of Mg-silicate gel; $R_{net} = R_{pre} - R_{dis}$
S	Reactive surface area (m^2) of the Mg-silicate substrates
υ	Stoichiometric coefficient of Si of the reactants and products of the reactions
$d^i si$	The amount of change (mol/kg) of the isotope i in the reactor at the time interval dt
dt	The time interval between two samplings during the experiment (seconds)
$\left(\frac{^i si}{^{total} si}\right)_{dis}$	The fractional abundance of $^i si$ in the experimental substrates
$\left(\frac{^i si}{^{total} si}\right)_{\bar{t}}$	The average fractional abundance (0 to 1) of $^i si$ in the experimental solutions between the sampling time interval
$\left(\frac{^{28} si}{^{29} si}\right)_{dis}$	The ratio of the abundance of $^{28} si$ to the abundance of $^{29} si$ in the substrates
$\left(\frac{^{28} si}{^{29} si}\right)_{\bar{t}}$	The ratio of the abundance of $^{28} si$ to the abundance of $^{29} si$ in the substrates in the experimental solutions between the sampling time interval
α_d	The kinetic fractionation factor for the Mg-silicate substrates dissolution
α_p	The kinetic fractionation factor for the Mg-silicate gel precipitation
r_{dt}	The true dissolution rate (mol/kg/s) of the Mg-silicate substrates taking account of the effect of Si fractionation
r_{pt}	The true precipitation rate (mol/kg/s) of the Mg-silicate gel taking account of the effect of Si fractionation
R_{exd}	The Si isotopic exchange rate caused by the Si fractionation of the dissolution
R_{exp}	The Si isotopic exchange rate caused by the Si fractionation of the precipitation

R_{dt}	The true dissolution rate (mol/m^2/s) of the Mg-silicate substrates taking account of the effect of Si fractionation
R_{pt}	The true precipitation rate (mol/m^2/s) of the Mg-silicate gel taking account of the effect of Si fractionation
$error_{dis}$	The relative error on the calculation of the dissolution rates taking account of the effect of Si fractionation
$error_{pre}$	The relative error on the calculation of the precipitation rates taking account of the effect of Si fractionation

abbreviation	
PDB	Principle of Detailed Balance
TST	Transition state theory

Table 2: The initial setting of the experiments

Names	Temperature	Substrates	Initial Si (mmol/kg)	Initial Mg (mmol/kg)	Initial pH (21/65℃)	Buffer
Precipitation Experiments; Si isotope composition: ^{28}Si (0.9223), ^{29}Si (0.0468), and ^{30}Si (0.0309)						
C	21.5℃	-	1.98	4.61	10.01	-
G	21.5℃	-	2.03	4.71	10.03	-
PDB Experiments; Si composition: ^{28}Si (0.0004), ^{29}Si (0.999), and ^{30}Si (0.0006)						
IJ	21.5℃	40 mg Mg-silicate gel	1.90	4.50	9.1	0.05 M $B(OH)_3$
IH	65℃	20 mg Mg-silicate gel	4.50	0.52	8.54/8.22	0.05 M $B(OH)_3$
IG	65℃	30 mg talc	4.50	0.52	8.54/8.22	0.05 M $B(OH)_3$

Table3. Fluid and calculated results of the PDB experiments.

Name	Time min	pH(20/65℃)	28Si mmol/kg	29Si mmol/kg	Si[b] mmol/kg	Mg mmol/kg	Na mmol/kg	SI(Talc)	SI(Sepiolite)	SI(Brucite)	SI(SiO_2(am)[c])	Log Q (Talc)	Rpre mol/m2/s	Rdis mol/m2/s	Rnet[d] mol/m2/s
IJ-0	0	9.1	0.01	1.90	1.91	4.50	18.83	13.40	13.55	-0.69	-0.07	35.90			
IJ-01	14	9.01	0.46	1.22	1.69	3.86	13.57	12.55	12.40	-0.92	-0.1	35.01	1.00E-11	7.43E-12	2.59E-12
IJ-1	26	9.03	0.60	0.78	1.39	3.67	12.91	12.26	11.96	-0.9	-0.19	34.72	1.02E-11	5.88E-12	4.29E-12
IJ-2[a]	63.5	9.02	0.85	0.61	1.49	3.71	13.16	12.34	12.08	-0.92	-0.16	34.80	1.79E-12	2.22E-12	-4.26E-13
IJ-3[a]	135	9.01	0.99	0.47	1.49	3.56	12.90	12.24	11.95	-0.95	-0.16	34.69	1.08E-12	1.09E-12	-9.11E-15
IJ-4	190	9.01	1.23	0.30	1.57	3.81	13.15	12.41	12.19	-0.93	-0.14	34.86	2.69E-12	2.93E-12	-2.43E-13
IH-0	0	8.54/8.22	0.00	4.50	4.50	0.52	17.14	11.40	10.46	-1.08	0.12	28.23			
IH-1	5	8.5/8.21	0.46	3.16	3.64	0.94	16.31	11.70	10.80	-0.86	0.03	28.89	9.94E-11	4.01E-11	5.93E-11
IH-2	10	8.47/8.21	1.35	2.50	3.90	1.20	15.35	11.97	11.18	-0.81	0.07	29.22	6.51E-11	8.30E-11	-1.79E-11
IH-3	15	8.48/8.17	1.45	2.03	3.53	1.19	15.56	11.73	10.84	-0.83	0.03	29.02	5.60E-11	3.09E-11	2.51E-11
IH-4	24	8.46/8.16	1.83	1.59	3.49	1.11	15.13	11.58	10.63	-0.88	0.02	28.84	3.50E-11	3.34E-11	1.61E-12
IH-5	35	8.47/8.16	2.07	1.34	3.48	1.04	14.83	11.49	10.52	-0.9	0.02	28.73	2.06E-11	2.04E-11	2.44E-13
IG-0	0	8.54/8.22	0.00	4.50	4.50	0.52	17.14	11.40	10.46	-1.08	0.12	28.23			
IG-1	1613	8.47/8.16	0.00	3.49	3.49	0.33	19.65	9.97	8.48	-1.42	0.02	26.69	2.84E-11	7.72E-26	2.84E-11
IG-2	4352	8.48/8.17	0.04	2.96	3.00	0.12	17.05	8.50	6.47	-1.82	-0.04	24.87	9.01E-12	8.00E-13	8.21E-12
IG-3	5812	8.46/8.15	0.05	2.70	2.74	0.10	16.93	7.80	5.78	-1.93	-0.08	24.32	8.24E-12	3.06E-13	7.94E-12
IG-4	8386	8.42/8.11	0.07	2.30	2.38	0.05	17.69	6.62	3.9	-2.32	-0.14	22.69	7.22E-12	7.14E-13	6.51E-12

[a] Calculated as the average values with similar values (^{28}Si and ^{29}Si) within the error

[b] Calculated as the sum of ^{28}Si, ^{29}Si,and ^{30}Si. ^{30}Si=0.0336×^{28}Si

[c] Amorphous Silica

[d] Rnet=Rpre-Rdis

Table 4 The maximum errors of the rates that simulated with a fractionation factor of 1.005.

α_p=1.005		
	Error R*p* %	Error R*d* %
IG	0.32	0.38
IJ	0.46	0.42
$\alpha_p=\alpha_d$ = 1.005		
	Error R*p* %	Error R*d* %
IG	0.38	0.42
IJ	0.57	0.53

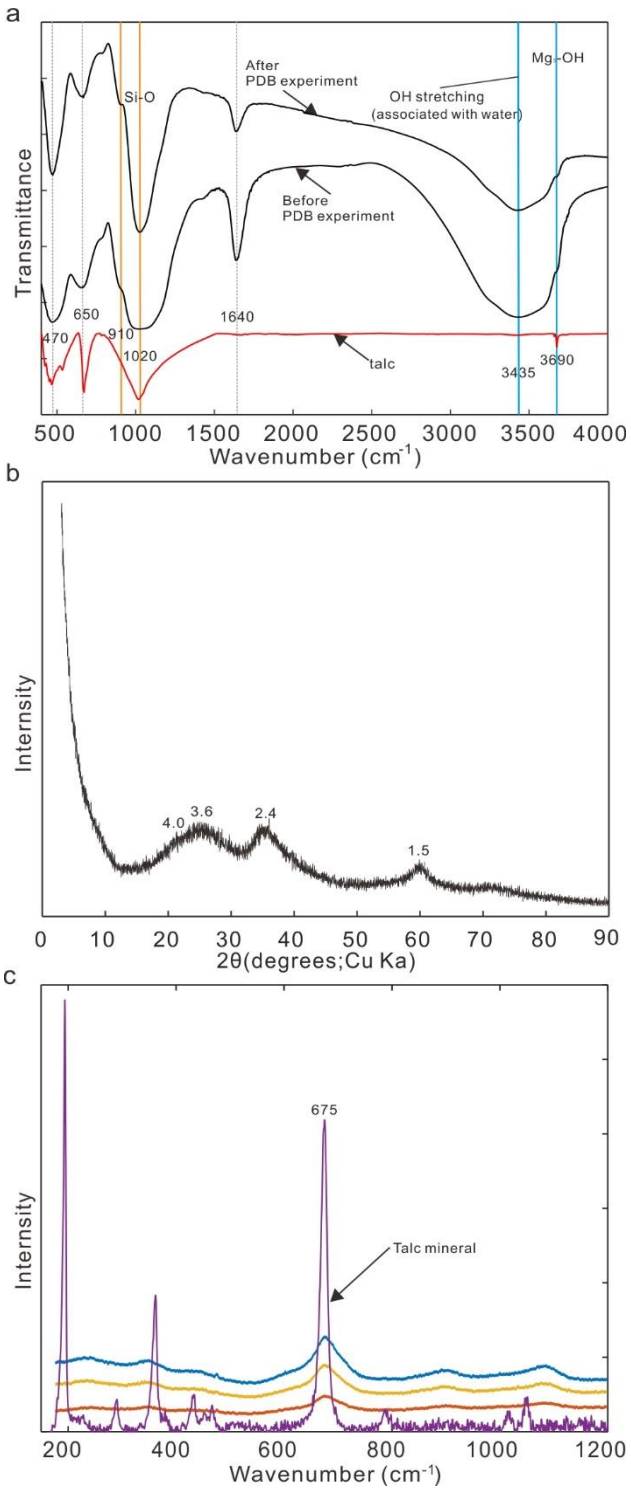

Figure 1 Results of solid analyses a) FTIR spectra of the Mg-silicate gels (before and after the PDB experiments at 65°C) and the talc substrates. Yellow solid lines illustrate the vibrations of the Si-O bond, blue solid lines indicate the OH bonds associated with H_2O or Mg, and grey lines are not diagnostic of the present phase; b) XRD analysis of the precipitates from precipitation experiments. c) Raman spectra of the mineral talc and precipitates from precipitation experiments.

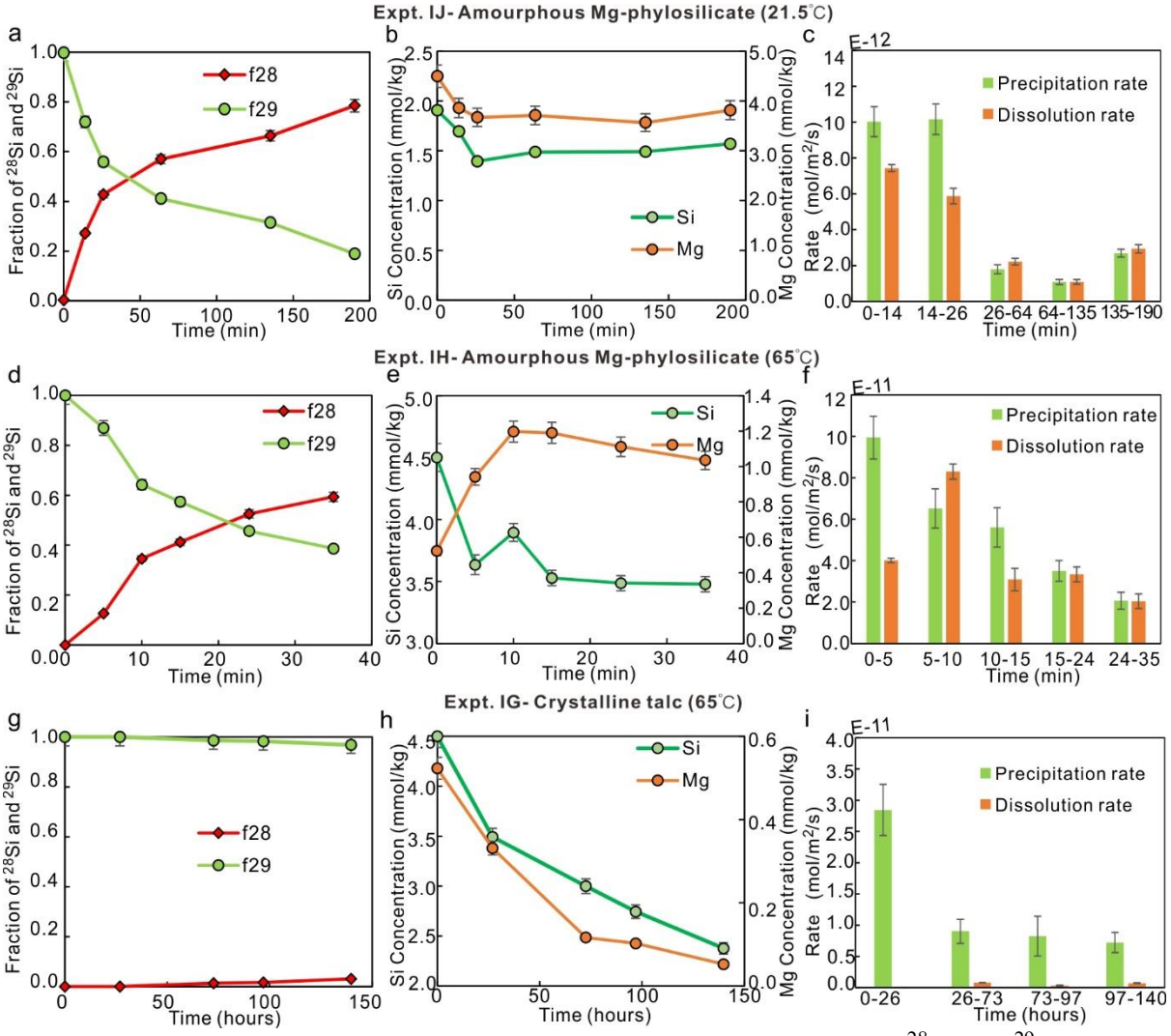

Figure 2 Fluid chemistry results from PDB experiments. The fraction of ^{28}Si and ^{29}Si, the concentration of Si and Mg, and rates of precipitation and dissolution of Expt. IJ (a-c), Expt. IH (b-e) and Expt. IG(f-i).

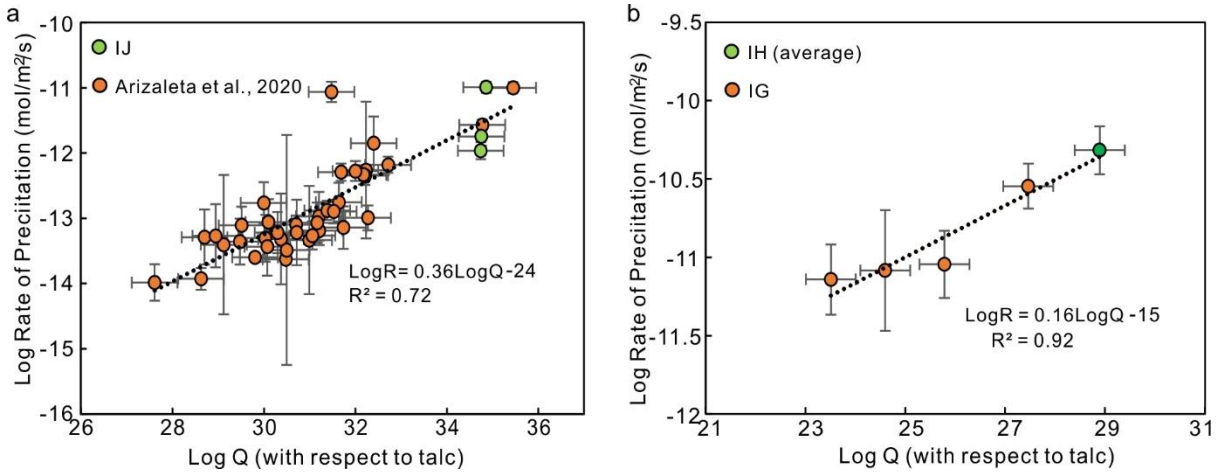

Figure 3 Logarithm of precipitation rates as a function of the logarithm of ion activity product (Q) calculated with respect to talc. a) Comparison between the precipitation rates from Expt. IJ and Arizaleta et al. (2020); b) Comparison of the precipitation rates from Expt. IH with that from Expt. IG.

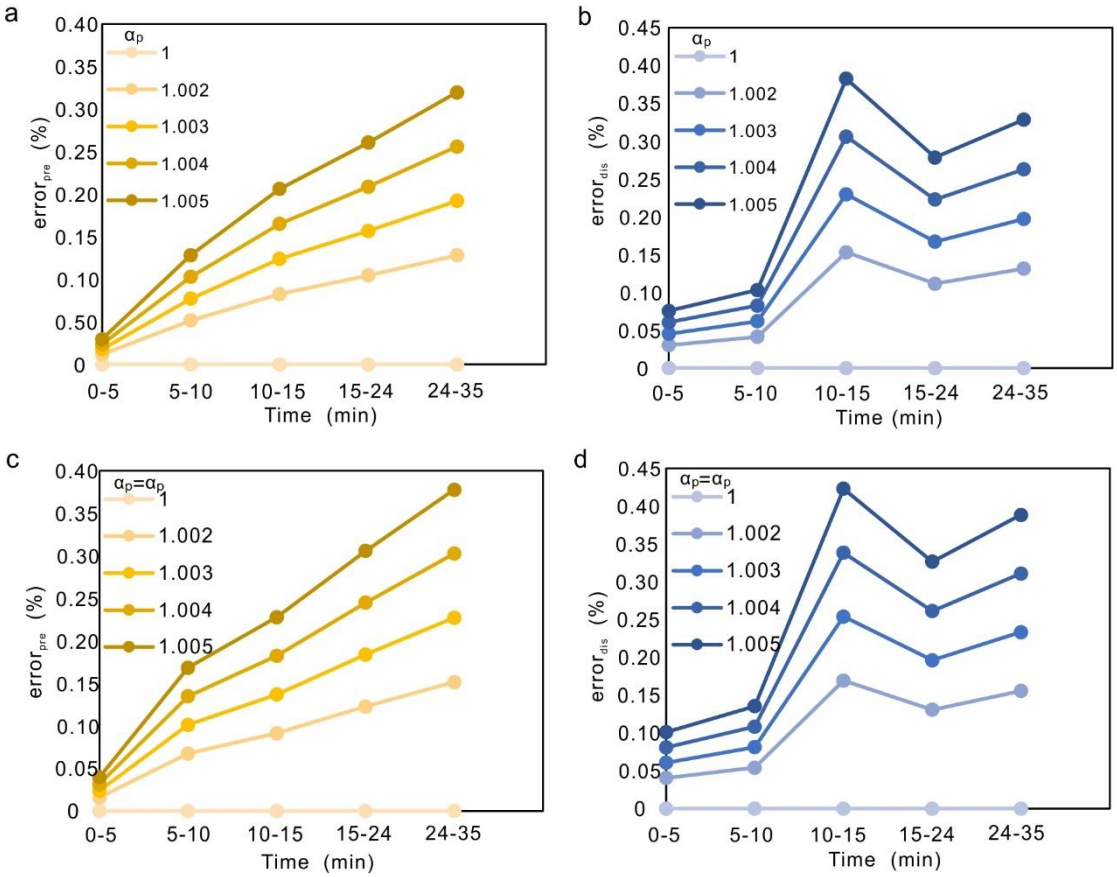

Figure 4: Simulation results of the effects of Si fractionation. a-b) The simulated errors (%) on the precipitation rates (a) and the dissolution rates (b) from Expt. IH with the isotopic fractionation only in the precipitation process. c-d) The simulated errors (%) on the precipitation rates (c) and the dissolution rates (d) from Expt. IH with the isotopic fractionation in both the precipitation and dissolution processes.

Appendix

Table S1 Si isotope fractions in mixing samples.

No	Solution[a]	f29[b] Expected	f29[b] QMS	Diff
1	100-0 mix	1.000	1.009	0.010
2	80-20 mix	0.814	0.824	0.010
3	60-40 mix	0.625	0.643	0.018
4	50-50 mix	0.530	0.547	0.017
5	40-60 mix	0.435	0.458	0.023
6	20-80 mix	0.242	0.251	0.009
7	0-100 mix	0.047	0.055	0.009

[a] % of the 29Si stock solution- % of the ICP standard solution

[b] f29=$^{29}Si/(^{28}Si+^{29}Si+^{30}Si)$

Table S2 Fluid chemistry from the precipitation experiments

Name	Time (hour)	pH	Si (mmol/kg)	Mg (mmol/kg)
C1	0.00	10.01	1.98	4.61
C2	41.87	9.32	1.01	3.95
C3	66.72	9.19	0.97	3.89
G1	0.00	10.03	2.03	4.71
G2	47.07	9.41	1.36	4.28
G3	93.65	9.32	1.31	4.27
G4	113.97	9.32	1.14	4.15

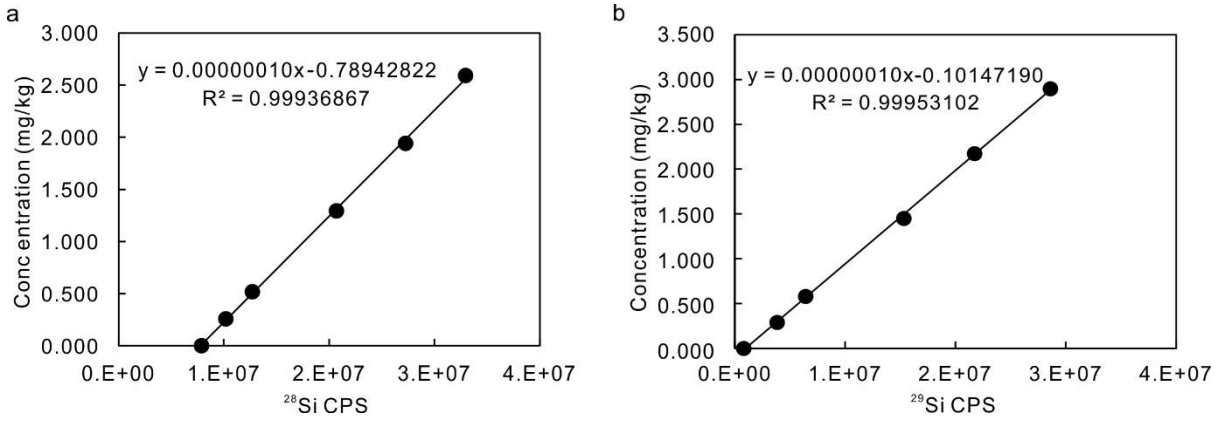

Fig S1 Standard calibration curves converting the signal intensities (cps) to the concentration of ^{28}Si (a) and ^{29}Si (b) for the mixing samples

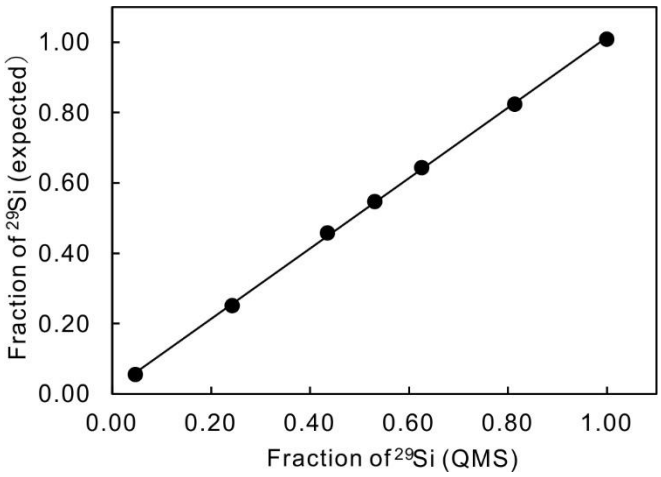

Fig S2 Comparison of the fraction of ^{29}Si from mixing samples between the expected and the Q-ICP-MS measurement. The

line shows a 1:1 relationship.

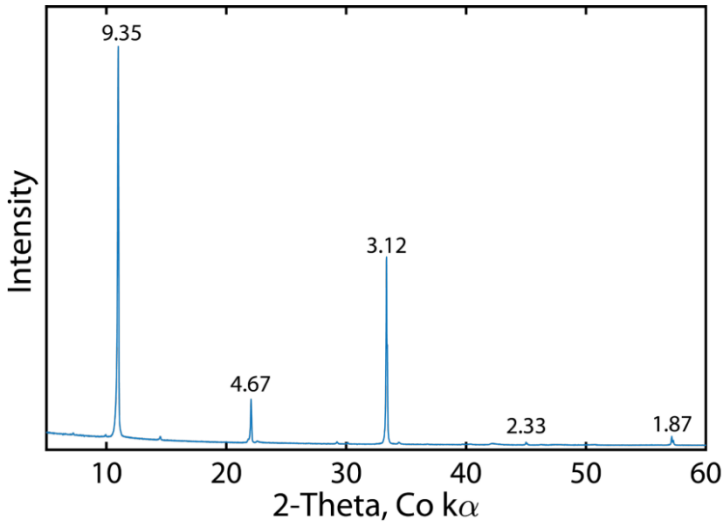

Fig S3 X-ray diffraction analysis of the crystalline talc used in the experiments.

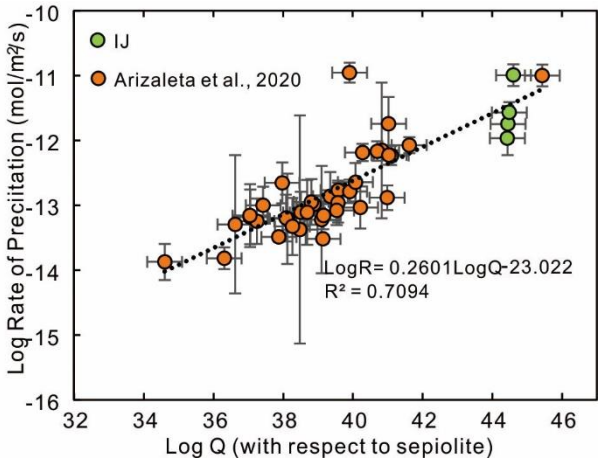

Fig S4 Logarithm of precipitation rates as a function of the logarithm of ion activity product (Q) to sepiolite from Expt. IJ and Arizaleta et al. (2020)